Image Formation in the Scanning Helium Microscope

A. Fahy [1,†], S.D. Eder[1,2,†], M. Barr[1], J. Martens[1], T.A. Myles[1] and P.C. Dastoor[1]

[1]*Centre for Organic Electronics, University of Newcastle, Callaghan, NSW 2308, Australia.*
[2]*Department of Physics and Technology, University of Bergen, Allégaten 55, 5007 Bergen, Norway.*
[†]*These authors contributed equally to this work.*
E-mail: adam.fahy@newcastle.edu.au

ABSTRACT

The scanning helium microscope (SHeM) is a new addition to the array of available microscopies, particularly for delicate materials that may suffer damage under techniques utilising light or charged particles. As with all other microscopies, the specifics of image formation within the instrument are required to gain a full understanding of the produced micrographs. We present work detailing the basics of the subject for the SHeM, including the specific nature of the projection distortions that arise due to the scattering geometry. Extension of these concepts allowed for an iterative ray tracing Monte Carlo model replicating diffuse scattering from a sample surface to be constructed. Comparisons between experimental data and simulations yielded a minimum resolvable step height of 67 ± 5 microns and a minimum resolvable planar angle of 4.3 ± 0.3 degrees for the instrument in question.

1. Introduction

Utilising a probe particle with Ångström-scale wavelength and milli-electron-volt energy, neutral helium atom microscopy is a surface-sensitive technique that results in no damage to the sample under investigation [1–3]. Helium atoms have long been utilised as a surface probe in helium atom scattering (HAS) [4,5] as they are uncharged, have no net spin and a low polarisability. The operation of such an instrument is based upon the illumination of a sample surface with a beam of ground state helium atoms, typically provided by a free-jet expansion [6]. Reflection mode imaging involves the detection of a portion of the backscattered signal, typically by ionisation followed by some form of mass selection. Currently there exists two configurations of neutral helium atom microscope, depending on the choice to use either a focusing element or a pinhole to define the size and shape of the spot on the sample surface [1,7,8]. Contrast arises due to the changes in the helium-surface interaction as a function of the surface topography, as well as the surface composition and arrangement [9].

Recent investigations using a pinhole-based instrument, referred to in the literature as the Scanning Helium Microscope (SHeM), have demonstrated that the technology is capable of exploiting both topological [7] and chemical [10] contrast modes. However, the underlying process of image formation within this specific instrument has yet to be fully described. The instrument detailed in [7] utilises a 90° scattering geometry where the detector is positioned to monitor the specular channel of the backscattered intensity. Such an arrangement was chosen for several reasons: to ensure reasonable signal levels, strong topological contrast, and to enhance the probability of energy transfer for chemical contrast studies. This scattering geometry influences the generated micrographs and offers the potential for additional information regarding the surface under investigation. For example, feature heights, gradients and other topological details could be extracted via quantitative analysis of the backscattered helium intensity.

Here we present a detailed study of the process of image formation for our pinhole SHeM with a 90° scattering geometry. In particular, the image distortions and possible occlusion of either the beam or detector aperture are examined, before the concepts are extended to yield estimates of the minimum resolvable difference in step heights and inclined planes through both experimental and modelled results. Knowledge of the specific limitations imposed by the scattering geometry of this instrument in terms of the smallest resolvable features is a fundamental requirement for advancing not only our understanding of topological contrast, but all of the available contrast mechanisms open to the technique.

Experimental Apparatus

The SHeM employed to collect the measurements presented has been detailed previously in the literature [7,11]. The system includes a free-jet expansion neutral helium beam source [1,11] with a 10 μm nozzle and is capable of stagnation pressures of up to 250 bar. The source assembly is mounted on a 3-axis manipulator, allowing for precise positioning relative to a sharp skimmer aperture (100 micron, Beam Dynamics Inc.). The centerline of the helium expansion extracted via the skimmer passes through a differential pumping stage before it is incident upon an aperture focused ion beam (FIB) milled into a silicon nitride membrane (Ted Pella part number 21525) forming the pinhole optics of the instrument. In particular, for the studies described herein a 5 μm pinhole was chosen, resulting a helium spot of Gaussian profile with a (6.9 ± 0.2) μm FWHM.

Figure 1 provides a sectioned schematic of the instrument's pinhole plate structure (which houses the pinhole and the detector aperture), and illustrates the interaction between the beam and the sample with the 90° scattering geometry. The xy plane (highlighted in blue in Figure 1) is located at the intersection of the incoming and outgoing beam-paths, hence defining a 'specular plane', analogous to the coincidence plane found in other microscopies. The specular plane forms the usual imaging position unless otherwise indicated and is situated at a distance of 2020 μm from the pinhole plate along the z-axis. A portion of the helium backscattered from the sample surface passes through the detector aperture, which subtends a solid angle of 0.1 sr at the specular plane. The detector itself consists of a HAL/3F PIC mass spectrometer (Hiden Analytical Inc.), housed in a close-fitted sheath chamber and is operated in stagnation mode. Stagnation detection refers specifically to the generation of a stable equilibrium of gas within the detector volume, based on the inflow of gas atoms and the outflow due to the fixed pump rate on the chamber. The mass spectrometer is set to select out ground-state helium at mass 4 AMU, and samples the stagnation volume once a stable population is reached.

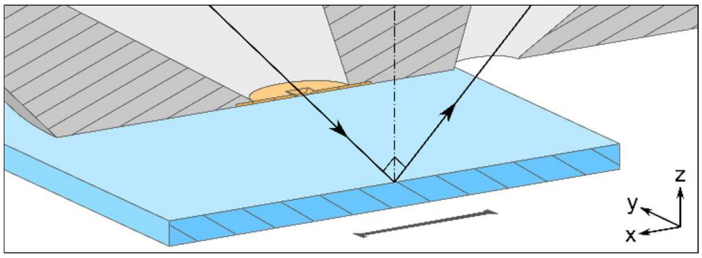

Fig. 1. Cross-sectional view of the SHeM scattering geometry. The helium beam, apertured by a pinhole cut into a silicon nitride membrane (orange), is incident on a sample (blue) at a relative angle of 45° with the backscattered beam collected through a detector aperture in the specular position. Scale bar represents 3 mm.

Image generation is accomplished by rastering the sample stage (aligned to sit parallel to the aforementioned specular plane) underneath the helium beam and recording the backscattered intensity at each position. With a 5 μm pinhole, calculated helium flux incident upon the sample is of the order 5 x 10^{10} atoms/second. Background gas arises from indirect, non-beam helium atoms in the sample chamber diffusing through to the detector (resulting in an instrument signal-to-background ratio of approximately 0.6). The resultant noise in the produced micrograph obeys Poisson statistics; higher noise levels typically indicate the presence of sub-resolution features of the sample surface.

2. Image Formation

The relationship between the incident beam, sample, and detector position has a direct consequence on the produced micrographs. Initial samples were chosen to have simple, well-understood architectures and - where possible - to be comprised of materials expected to predominantly scatter diffusely (through numerous topological features below the lateral resolution of the instrument, as dictated by the helium beam spot size and profile). Efforts were also made to limit count rate differences arising due to dissimilar materials; however, it has already been shown that contrast arising due to the chemistry of the material is orders of magnitude smaller than those observed from topological features [10] and thus contributes negligibly to the image.

2.1. Beam Occlusion

To understand image formation, it is useful to first examine how beam occlusion can occur in the SHeM. Taking conventions from microfacet theory [12] (used in the modelling of, among other things, the diffuse scattering of light from surfaces), we can divide occlusion into two general categories: shadowing and masking. Shadowing occurs when a section of the sample surface is not visible to the incident beam direction (and thus does not contribute to the backscattered response), while masking occurs when the surface is not visible in the view direction - that is, not within line-of-sight of the detector.

Figure 2 demonstrates clear examples of both forms of occlusion through a TEM grid suspended over a stainless steel sample slide. Note that in this micrograph (and all others within this paper), the helium beam enters from the right-hand side, with the backscattered helium collected by the detector situated on the left. As is observed in secondary electron images in the scanning electron microscope (SEM), in the SHeM micrographs samples appear to be illuminated from the detector position. The dark regions within the micrograph indicate masked areas of the sample - for instance, the silhouette of the grid on the substrate, and the right hand edges of the stepped TEM grid surface. In these positions, the helium beam has struck the sample surface but the backscattered atoms have been unable to reach the detector. For the orientation of the SHeM micrographs discussed in this paper, masked areas will always appear to the right of the feature that caused the occlusion. With regards to shadowing, the pixels showing the TEM grid constitute positions where the incident beam was prevented from striking a lower section of the sample surface. Note that the stainless steel sample slide substrate is positioned in the specular plane for the micrograph in Figure 2, and appears brighter than the copper TEM grid due to the latter having a large number of surface features (resulting in highly diffuse scattering).

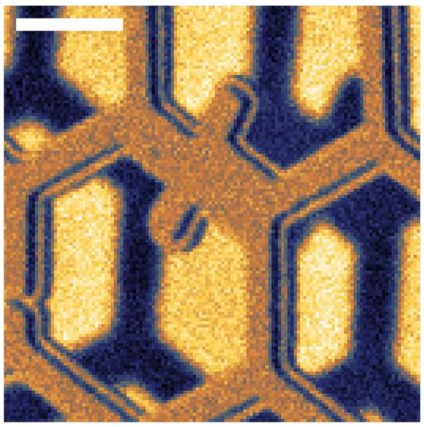

Fig. 2. SHeM micrograph of a hexagonal TEM grid suspended off the surface of a stainless steel sample slide. Image collected using a 3 micron step size; scale bar 100 microns in length. The micrograph demonstrates both *shadowing* and *masking* - instances where either the beam or the detector is occluded (respectively). The dark regions on the substrate in the micrograph indicate masked regions, whereby the incident beam has struck the surface but the backscattered helium is prevented from reaching the detector aperture by the raised TEM grid. Similarly, the actual TEM grid surface can be considered an instance of shadowing - the TEM grid is blocking the beam from reaching a section of the substrate below.

2.2. *Beam Projection - Theory*

Further expanding on how sample geometry affects the produced images, we can consider projections of the sample surface along both the beam and detector axes. Figure 3 demonstrates the principle with a highly simplified sample geometry. To understand the effect of beam geometry, the beam can be thought to project an image of the sample onto the specular plane, which is then collected in one-to-one correspondence by the detector. Faces hidden from the incident beam are shadowed, and hence will not contribute to the final micrograph. Similarly, one can repeat the process from the detector perspective, with anything not visible considered to be masked in the final image.

In the x-axis, the incident beam striking the sample surface at 45° has specific consequences with regards to the produced micrographs. Areas of the sample not parallel to the specular plane will experience 'projection distortion', causing their apparent length to vary as a function of the relative angle with respect to the beam (or equivalently, with respect to the specular plane – θ in Figure 3). However, unlike SEM (for example) where the apparent length of a feature can only be contracted (foreshortening [13]), projection distortion for the SHeM can result in not only contraction but stretching as well. The apparent length of the needle in Figure 3 (the size of the shadowed region) can be seen to exhibit such behaviour as the value of θ is varied from 0° through to 180°. Considering the geometry as shown in Figure 3, one can use trigonometry to define a scaling factor (SF) that will convert the true length of a feature into the apparent length in a SHeM micrograph. Defining θ as before (the relative angle between a feature and the specular plane), and α as the angle of the incident beam relative to the specular plane normal, a linear feature in a SHeM micrograph will be distorted according to the relationship:

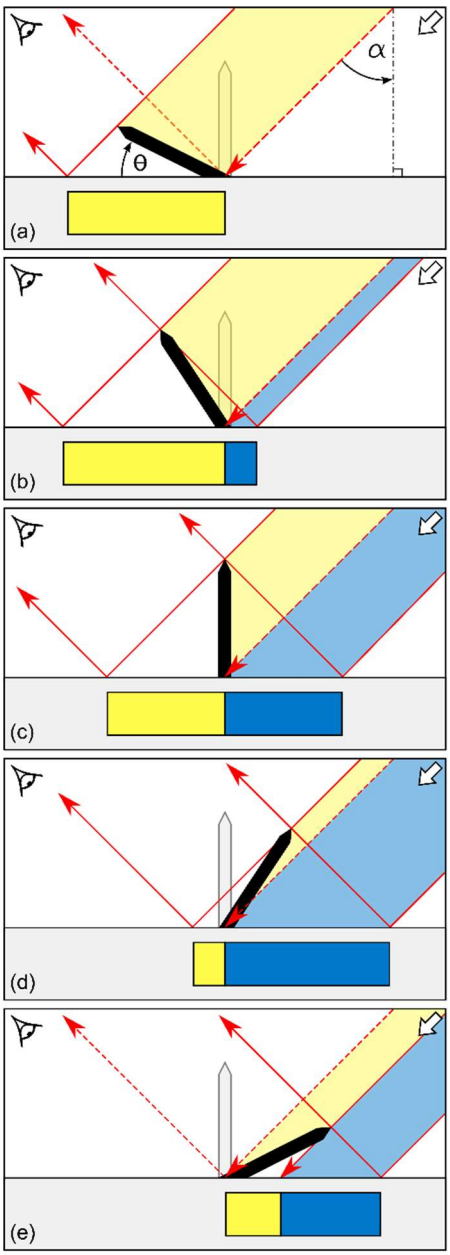

Fig. 3. Depiction of the incident helium beam entering from the right interacting with a simple sample (a needle) mounted on a flat plane (specular plane), along with the specular reflections from the plane to the detector positioned to the left (i.e.: where the instrument is 'looking' at each scan position). Yellow indicates a shadowed region (areas where beam atoms cannot directly strike the surface), while blue represents masking (regions where the backscattered atoms do not reach the detector). As the angle θ between the needle and the specular plane increases from 0° through to 180° as shown in (a) through (e), the apparent length of the sample (the shadowed region) can be seen to change dramatically. When the needle sits normal to the specular plane as in (c), the 90° geometry means that the apparent length of the sample matches the true length. Note also that once θ moves past 135° as in (e), the shadowed region will appear to reverse direction, with the opposite side of the needle now exposed to the incident helium beam.

$$SF = cos(\theta) + sin(\theta) \cdot tan(\alpha). \qquad (1)$$

For a system with α = 45°, equation (1) then simplifies to:

$$SF = sin(\theta) + cos(\theta). \qquad (2)$$

Figure 4 shows a plot of the scaling factor given in equation 2 as a function of θ between 0° and 180°. A plane tilted away from the incident beam (0° < θ < 90°, Figures 3(a) and (b)) will appear longer than its true length in a SHeM micrograph, while those tilted towards the beam (90° < θ < 180°, Figures 3(d) and (e)) will appear shorter. Negative values of the scaling factor (135° < θ < 180°) indicate the apparent length of the plane has reversed direction, relative to the incident beam. Such an instance can be seen in Figure 3(e), with the opposite side of the needle now under illumination from the helium beam and the resulting shadow appearing on the beamward side of the needle base.

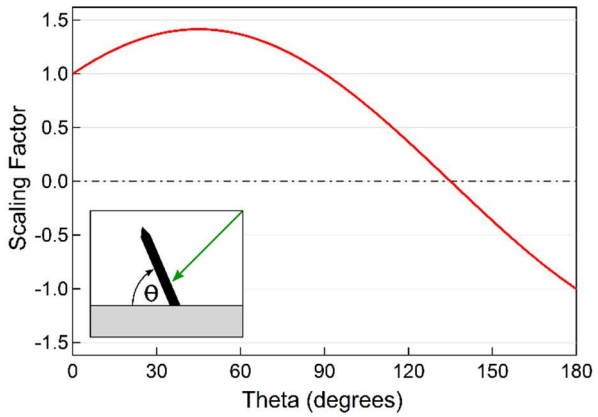

Fig. 4. Plot of the scaling factor as defined in equation 2 for a plane at an angle θ with respect to the specular plane (see inset). Note that this scaling factor will only apply in the horizontal (x) scan axis – in the vertical direction the image will be in direct correspondence with the sample.

2.3. Beam Projection - Experiment

A 5 millimeter square silicon frame of 200 micron thickness, in the center of which sits a 250 micron square silicon nitride membrane of thickness 10 nm (Norcada part number NX5025Z) was imaged, since it offers a well-defined geometry. Figure 5 shows the sample dimensions, along with a SHeM micrograph of the membrane (micrograph taken with the frame positioned in the specular plane). The top surface of the silicon frame retains its square shape, with all sides measuring 550 microns in length within experimental error (taken as twice the scan step size, namely ±20 microns). However, the sloped faces running from the frame down to the central membrane are distorted depending on their orientation relative to the incident beam and detector apertures. In particular, the distortion of the image along the plane of the beam and detector (horizontal axis in the micrograph) is clear through comparison of the apparent size of the inclined planes down to the central membrane.

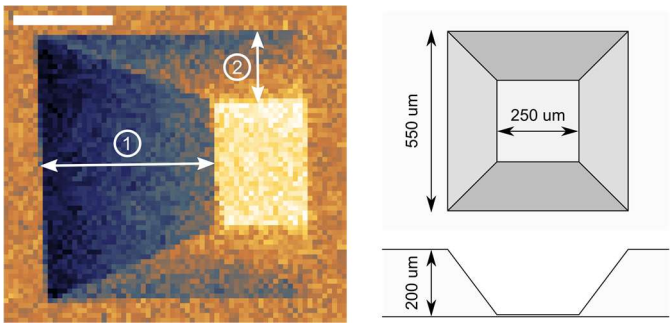

Fig. 5. SHeM micrograph of the central portion of a silicon nitride x-ray window, with the dimensions of the window shown in the schematic on the right. Micrograph collected using 10 micron step size; scale bar is 200 microns in length.

Based on the geometry of the window, the distance from the outer frame edge to the membrane as viewed from above should be 150 microns. In the vertical axis, this separation (arrow '2' in Figure 2) is confirmed in the SHeM micrograph. However, in the horizontal axis (arrow '1') the distance has been distorted due to the inclination of the plane with respect to the beam. In particular, shadowing causes a 'cropped' appearance of the square central membrane in the micrograph. The faces leading down to the membrane are inclined with respect to the specular plane by approximately 53°; greater than the 45° inclination of the incident helium beam. Consequently, one of the faces and part of the central membrane are completely hidden from view of the beam, and subsequently do not contribute to the produced image. In addition, the micrograph of the silicon nitride membrane provides a ready test of the scaling factor shown in Figure 4. Application of the scaling factor to the face indicated by arrow '1' (true length of 250 microns) yields an apparent length of 350 microns, in excellent agreement with the (350 ± 20) microns determined from the micrograph.

2.4. Complex 3D Structures

The next step in the study of image formation within the instrument focused on a fully 3D sample that maintained a clear and simple structure. Sugar crystals belong to the monoclinic crystal system [14] and, dependent on the impurities present, form features of a size amenable to producing detailed images within the current generation of the SHeM. SEM images of such crystals show high levels of asperities with sizes down well below the current resolution of the SHeM, and so diffuse scattering from the surface is assured. Figure 6 shows the SHeM micrograph of such a sugar crystal, with the substrate upon which it rests positioned in the specular plane.

With the dominance of diffuse scattering from the crystal facets, the scattered helium is emitted primarily in a cosine distribution centered about the normal to each surface and independent of the incident beam angle. It follows then that the top of the crystal (face '1') will reflect the most into the detector. The facets indicated by '2' have smaller mean intensity values as compared to the top face as dictated by their relative tilts towards the detector aperture. The darkest facet ('3') has its surface normal facing back towards the incident beam, leading to the minimum of scattered atoms making their way to the detector from this position. Interestingly, the face below this ('4') has a greater mean intensity,

despite being completely hidden from view of the detector. For this face, multiple scattering events (that is, instances where the incident helium atom undergoes multiple surface interactions before detection) raise the count rate above that of faces in direct view of the detector. The helium beam strikes the face, is scattered back towards the carbon substrate, and a secondary scattering event leads to some of this helium entering the detector volume. Such instances of multiple scattering leading to unexpected intensities can be found across a large number of SHeM images [1,7,10]. The consequences of the multiply scattered atoms is a complex question, and more work is needed to account for its effects in the produced images.

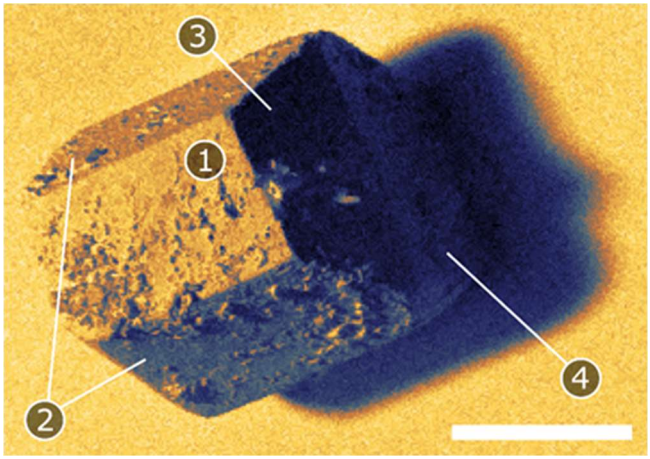

Fig. 6. SHeM micrograph of a sugar crystal (*sucrose*) adhered to a carbon dot. Image collected with 6 micron steps; scale bar 500 microns in length.

3. Minimum Resolvable Step Height

The lateral resolution in the SHeM is solely dependent on the size and shape of the beam spot profile projected onto the sample surface. However, the scattering geometry will directly affect the height resolution observed in a SHeM micrograph. If the difference in signal (number of helium atoms entering the detector aperture per unit time) recorded from two different parallel planes does not exceed the noise level, the features will not be observed in the subsequent SHeM micrograph. As an illustrative example, in the sugar crystal presented in Figure 6, the top face (1) shows identical count rates (to within the noise) to the carbonaceous substrate. Despite the considerable height differences between these features, it is in fact the presence of the edges of the crystal face that allow the observer to distinguish the top of the crystal. Much the same as the materials present in Figure 2 result in different count rates for parallel planes, in Figure 6 the material differences yield very similar count rates between the top face and the substrate.

In order to quantify the minimum resolvable step height, a 3D printer (Formlabs Form 2 3D stereolithography printer) was used to fabricate a sample structure consisting of a series of well-defined stepped terraces from an optically transparent resin (RS-F2-GPCL-04). As shown in Figure 7, the 3D printed structure consisted of a series of terraced steps of heights 500 µm, 250 µm, 100 µm, 75µm, 50 µm, 25 µm, 15 µm and 10 µm (±10 µm). SEM micrographs (Figure 7 insets) revealed that the sample had an inherent fine scale surface roughness from the print process that produces primarily diffuse scattering of the incident helium beam. Furthermore, the homogeneous nature of a 3D printed sample avoids any issues with material disparities obscuring the source of the differences in collected signal.

Varying the distance of a sample from the specular plane will result in alterations to not only the raw signal at the detector aperture, but also the background observed. These alterations arise due to the complex interplay of several factors, including multiple scattering and changes in the detector subtended angle. The 3D printed set of terraces offers the benefit of allowing for the collection of a quantitative measurement of the background, whilst simultaneously allowing for the measurement of signal from steps at different z-positions. The background count rate was collected via the mean value of the masked region at the base of the tallest step, which represents a position whereby the backscattered helium beam is prevented from directly entering the detector aperture. The micrographs collected of the 3D printed sample were recorded under typical instrument operating conditions, namely a beam stagnation pressure of 200 bar, a beam stagnation temperature of 298 K and a 5 µm pinhole as the final optical element. Count rates whilst collecting the micrograph were of the order 1.5 kHz, with a signal-to-noise ratio of ~23 (calculated as in [7]) with the sample at the specular plane (raw count rates and signal-to-background ratios as a function of z-distance appear in Appendix A).

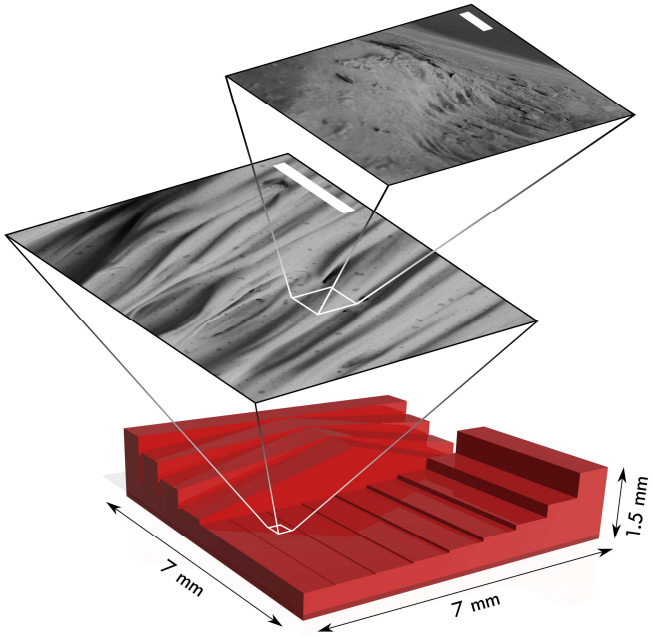

Fig. 7. Model of the 3D printed sample designed for use in determination of the minimum resolvable step height. Inserts show SEM micrographs of the printed material with feature sizes apparent well below the lateral resolution of the SHeM used in the work presented. Scale bars are 30 and 2 microns in length respectively.

Figure 8(a) shows the SHeM micrograph of the 3D-printed sample. Note that due to the distortions detailed previously, each step will shadow a portion of the subsequent step, causing an apparent variation in the width of each feature. The Michelson contrast (M) between two regions can be calculated using

$$M = \frac{I_A - I_B}{I_A + I_B}, \qquad (3)$$

where I_A and I_B are the mean count rates on regions A and B, respectively. Michelson contrast values (Figure 8(c)) were determined between consecutive steps by taking the mean count at each step, subtracting the background signal (calculated as mentioned above), and comparing the background-subtracted values using equation 3.

To confirm the source of the contrast, an iterative ray tracing Monte Carlo model was constructed in MATLAB, replicating diffuse scattering from a sample surface under a 45° incident beam (90° scattering geometry). Rays are projected from the pinhole onto the sample at 45°, whereby they are radiated back towards the pinhole plate via a cosine distribution [15]. Rays entering the detector aperture are counted and, upon the final iteration of the model, are compared with the total number of rays fired. Rays not entering the detector aperture are disregarded (thus allowing the simulation to be directly compared with the experimental results). To replicate the experimental scattering geometry, the sample is modelled as a flat surface positioned at the specular plane. The different step heights are then simulated by adjusting the separation between the pinhole plate and the modelled sample surface along the z-axis (see Figure 1). Michelson contrast values were calculated based on the simulated count rates, with these contrast values then used to construct a virtual SHeM image for comparison with the experimental micrograph. Both the simulated contrast values and the derived micrograph are shown in Figure 8(b) and (c), alongside the experimental results.

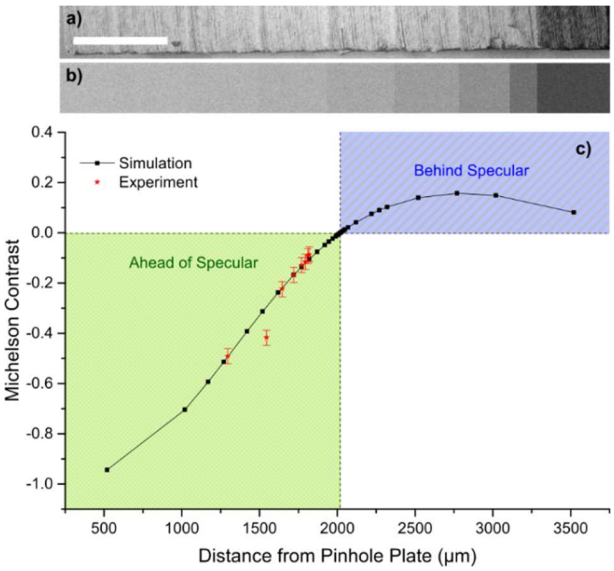

Fig. 8. (a) SHeM micrograph of the 3D printed step sample, collected using a 10 micron step; scale bar 1000 microns in length. (b) Virtual SHeM image of the same structure constructed from the results of the Monte Carlo simulation. (c) Plot of the experimental and theoretical Michelson contrast values for adjacent steps. As indicated by the vertical dashed line, the specular plane of the instrument is located at a distance of 2020 microns from the pinhole plate, thus allowing distinction between positions ahead of and behind specular (see shaded regions).

Despite the simplistic nature of the scattering in the Monte Carlo model, the simulated results produced are in good agreement with the experimental results. It should be noted that additional experimental data points were collected using different working distances and have produced results consistent with the plot above. The 45° incident beam and therefore presence of a specular position leads to a more rapid Michelson contrast change when moving ahead of specular (i.e.: towards the pinhole plate) in comparison to moving behind specular. With regards to the latter, there exists a contrast 'dead zone' over a relatively broad range of step heights in the region of 2000 - 3000 μm away from the pinhole plate. While moving towards the pinhole plate shows stronger contrast changes over all step heights simulated, the probability of occlusion increases, hence limiting samples exhibiting large aspect ratios. Imaging is therefore a delicate balance between available contrast and image formation, as described in Section 2.

The minimum resolvable step height is the point at which the difference in count rate between two steps is less than the uncertainty in the measurement. In practice, this means that using the Michelson contrast equation (equation 3) and performing propagation of uncertainty with the standard deviation derived from the SHeM micrograph will yield a contrast value threshold at which surface features become ambiguous. Under the standard operating conditions used for this experiment, the threshold contrast value was found to be 0.03. Consequently, the Monte Carlo model predicts that the minimum resolvable step height for flat planes is (67 ± 5) μm under the aforementioned standard conditions with the reference plane at the specular position. Based on the minimum resolvable step height being of the order of 70 microns, differences between the lowest four sample steps in the SHeM micrographs should not be discernible. Inspection of inset (a) in Figure 8 agrees with this assertion, with the apparent intensities between the referenced steps being identical within the noise present. It is then of interest that despite the similarities in intensity, the edges of the steps are still recognisable. The nature of the 3D print, namely the presence of a lip at the edge of each step (confirmed via a Dektak XT stylus profilometer) is the cause of the observed boundaries between adjacent steps. Changes in the mean plane angle, as present at these boundaries, results in contrast higher than that stemming from the step heights, and hence the edges are visible in the produced micrograph. Due to the absence of such lips in the simulated images, the edge boundaries are not reproduced in Figure 8(b).

The employed definition for a contrast threshold based on the noise present in the SHeM micrograph will obviously depend on the collection time per pixel. Long collection times will reduce this smallest resolvable step height to a certain extent, notably at the expense of image recording time. Furthermore, large pixel counts will render contrast differences of the order of this threshold still amenable to detection within the image. As noted in the literature [16,17] the primary concern for instruments utilising neutral helium is detector sensitivity and the associated count rate limitations. Increases in detector sensitivity will allow for an increase to the recorded intensity or pixel density, and hence improve the resolution. Note that compared to charged particle probe- and photon-based instruments, long collection times under a helium beam will not result in sample degradation.

4. Minimum resolvable planar angle

To investigate the effects of mean plane angle on image contrast observed in the SHeM (such as that observed at the lips of the step edges), a series of sloped planes (0°, ±5°, ±10°, ±15°) were fabricated alongside the steps (see Figure 7). To account for the sloped planes in the experimental setup, the aforementioned Monte Carlo model was modified to allow the sample to be tilted out of parallel with the pinhole plate. The resultant SHeM and simulation data are shown in Figure 9.

Unlike in the experiments involving the minimum resolvable step height, it is more difficult to decouple the contrast induced by both angle and step height in the experimental data. As can be observed in the SHeM image in Figure 9(a), there is an obvious contrast gradient across each angled face due to the increasing separation from the pinhole and detector apertures. To minimise the effect of height change across the planes, the experimental evaluation of the Michelson contrast was performed by collecting count rate data from areas close to the ridge at the intersection of the two planes. Knowledge of the scaling factor (shown in Figure 4) allowed for regions of equal distance from the pinhole plate to be used for the collected signal. Note that all Michelson contrast values were calculated with respect to a flat surface located at the specular plane of the instrument.

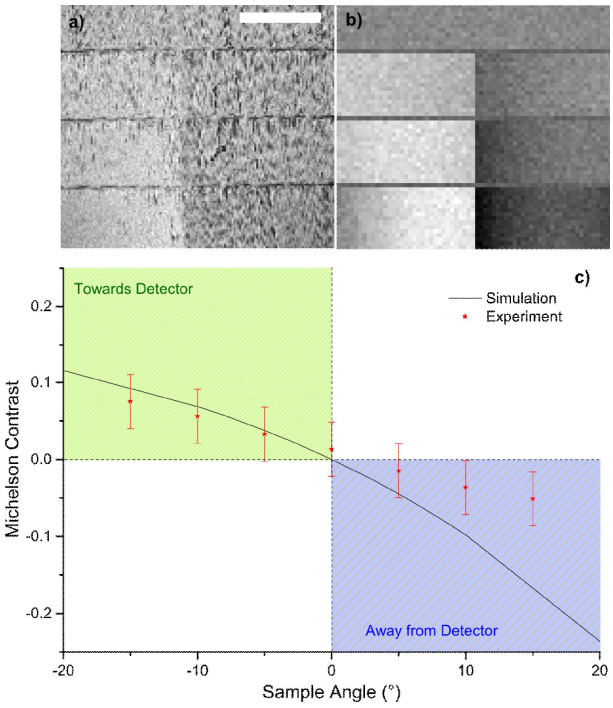

Fig. 9. (a) SHeM micrograph of the 3D printed angled planes. Image collected using a 25 micron step; scale bar 1000 microns in length. (b) Virtual SHeM image of the same structure constructed from the results of the Monte Carlo simulation. (c) Plot of the experimental and theoretical Michelson contrast values for the angled planes.

As with the step height analyses, there is qualitative agreement between the experimental and the simulated data. Multiple scattering begins to dominate image contrast for facets facing further away from the detector aperture. As such, the angled planes directed away from the detector will behave similarly to face '4' in Figure 6. Due to the absence of multiple scattering events from the Monte Carlo model, there will be a progressive divergence between model and experiment as observed in Figure 9(c). A more sophisticated simulation of the scattering geometry including the effects of multiple scattering is thus required in order to address the influence it has on the produced micrographs and hence move towards real quantitative contrast analysis.

Due to the specifics of the 3D printing used to fabricate the sample, the angled planes showed a marked increase in surface roughness as compared to the flat planes. As such, the experimental uncertainties in the SHeM micrograph were found to be larger than those for the step height sample, and a corresponding threshold contrast value of 0.035 was derived. In the same manner as for the step heights, using the Monte Carlo model and the experimental threshold we conclude that the minimum resolvable planar angle for the instrument is 4.3 ± 0.3°. We find the calculated result is in good agreement with the SHeM micrographs (Figure 9(a)), wherein the 5 degree plane is difficult to distinguish from the flat plane with the exclusion of edge effects.

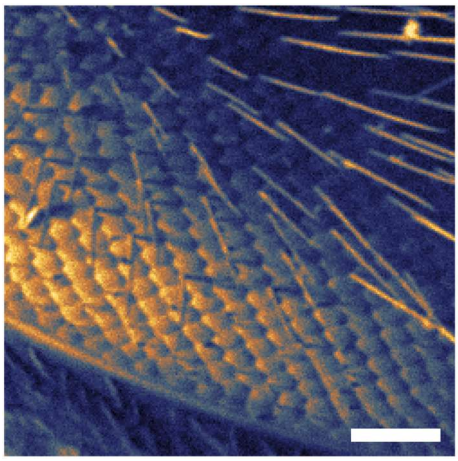

Fig. 10. SHeM micrograph of an eye of a honey bee (*Apis Melifera*). Image collected using a 2 micron step; scale bar 100 microns in length. The changing angle of the surface under investigation yields significantly more contrast than any relative changes in height, despite the extent of the latter.

The investigation into the series of sloped planes shows that the SHeM is much more sensitive to changes in angle than it is to height. As such, the SHeM excels at imaging samples demonstrating small angular variations across the surface (as may be present in biological samples and thin membranes), even in the absence of sharp changes in sample height. Figure 10 shows a SHeM micrograph of a section of honey bee eye (*Apis Melifera*) which includes a large variation in height across its curved surface. Despite the difference in height, it is the small changes in angle at the edges of the facets which yields significant contrast and results in an intuitive image. As a complicated biological sample, the micrograph presented in Figure 10 also exhibits all of the image formation effects discussed previously, including projection distortion, instances of occlusion, and multiple scattering.

5. Conclusions

We have demonstrated basic image formation within the SHeM, and subsequently derived estimates for the minimum resolvable step height and planar angle of the instrument under standard operating conditions, with values of 67 ± 5 μm and 4.3 ± 0.3°, respectively. Furthermore, the developed knowledge of a number of aspects of the image formation process has allowed for the implementation of a Monte Carlo model that shows strong agreement with the experimental results. With work ongoing with respect to modelling and optimising neutral beam optics [18–20], the potential exists for the development of a so-called 'virtual SHeM'. Refinement of this virtual SHeM, along with a higher-sensitivity helium detector, will allow us to improve the current instrument (namely with regards to lateral, step height and angular resolution), and to tailor subsequent helium microscopes for specific imaging requirements.

Acknowledgements:

This research was supported by the Australian Government through the Australian Research Council's Discovery Projects funding scheme (project DPDP170103979). SDE has received funding from The Research Council of Norway through a FRIPRO Mobility Grant (contract no 250018/F20). The FRIPRO Mobility grant scheme (FRICON) is co-funded by the European Union's Seventh Framework Programme for research, technological development and demonstration under Marie Curie grant agreement (No. 608695). Postgraduate research scholarships (TAM) from the University of Newcastle gratefully acknowledged. The work was performed in part at the Materials node of the Australian National Fabrication Facility, a company established under the National Collaborative Research Infrastructure Strategy to provide nano and microfabrication facilities for Australia's researchers. We thank N. P. Holmes for assistance in collecting the SEM micrographs at the University of Newcastle Electron Microscopy and X-ray Unit.

Appendix A: Supplementary Material

Supplementary data related to this article can be found at the end of this document.

References:

[1] M. Barr, A. Fahy, A. Jardine, J. Ellis, D. Ward, D.A. MacLaren, W. Allison, P.C. Dastoor, A design for a pinhole scanning helium microscope, Nucl. Instruments Methods Phys. Res. Sect. B Beam Interact. with Mater. Atoms. 340 (2014) 76–80. doi:https://doi.org/10.1016/j.nimb.2014.06.028.

[2] S.D. Eder, A.K. Ravn, B. Samelin, G. Bracco, A.S. Palau, T. Reisinger, E.B. Knudsen, K. Lefmann, B. Holst, Zero-order filter for diffractive focusing of de Broglie matter waves, Phys. Rev. A. 95 (2017) 23618. doi:10.1103/PhysRevA.95.023618.

[3] P. Witham, E. Sanchez, A simple approach to neutral atom microscopy, Rev. Sci. Instrum. 82 (2011) 103705. doi:10.1063/1.3650719.

[4] G. Bracco, B. Holst, Surface Science Techniques, in: G. Bracco, B. Holst (Eds.), Springer, 2013: pp. 333–367.

[5] D. Farìas, K.-H. Rieder, Atomic beam diffraction from solid surfaces, Reports Prog. Phys. 61 (1998) 1575. http://stacks.iop.org/0034-4885/61/i=12/a=001.

[6] Scoles, Atomic and Molecular Beam Methodes, Oxford University Press, New York Oxford, New York Oxford, 1988.

[7] A. Fahy, M. Barr, J. Martens, P.C. Dastoor, A highly contrasting scanning helium microscope, Rev. Sci. Instrum. 86 (2015) 23704. doi:10.1063/1.4907539.

[8] M. Koch, S. Rehbein, G. Schmahl, T. Reisinger, G. Bracco, W.E. Ernst, B. Holst, Imaging with neutral atoms-a new matter-wave microscope, J. Microsc. 229 (2008) 1–5. doi:10.1111/j.1365-2818.2007.01874.x.

[9] D.A. MacLaren, B. Holst, D.J. Riley, W. Allison, Focusing Elements and Design Considerations for a Scanning Helium Microscope (SHeM), Surf. Rev. Lett. 10 (2003) 249–255. doi:10.1142/S0218625X03005062.

[10] M. Barr, A. Fahy, J. Martens, A.P. Jardine, D.J. Ward, J. Ellis, W. Allison, P.C. Dastoor, Unlocking new contrast in a scanning helium microscope, Nat. Commun. 7 (2016) 10189.

[11] M. Barr, A. Fahy, J. Martens, P.C. Dastoor, A simple counter-flow cooling system for a supersonic free-jet beam source assembly, Rev. Sci. Instrum. 87 (2016) 53301. doi:10.1063/1.4948391.

[12] M. Oren, S.K. Nayar, Generalization of Lambert's reflectance model, in: Proc. 21st Annu. Conf. Comput. Graph. Interact. Tech. - SIGGRAPH '94, ACM Press, New York, New York, USA, 1994: pp. 239–246. doi:10.1145/192161.192213.

[13] J. Goldstein, D.E. Newbury, P. Echlin, D.C. Joy, C.E. Lyman, E. Lifshin, L. Sawyer, J.R. Michael, Scanning Electron Microscopy and X-Ray Microanalyses, 3rd ed., Springer Science-Buisness Media, LLC, 2003.

[14] F.E. Young, F.T. Jones, H.J. Lewis, D-Fructose–Water Phase Diagram, J. Phys. Chem. 56 (1952) 1093–1096. doi:10.1021/j150501a015.

[15] J. Greenwood, The correct and incorrect generation of a cosine distribution of scattered particles for Monte-Carlo modelling of vacuum systems, Vacuum. 67 (2002) 217–222. doi:10.1016/S0042-207X(02)00173-2.

[16] R.B. Doak, The assessment of field ionization detectors for molecular beam use, J. Phys. Condens. Matter. 16 (2004) S2863–S2878. doi:10.1088/0953-8984/16/29/002.

[17] A.R. Alderwick, A.P. Jardine, H. Hedgeland, D.A. MacLaren, W. Allison, J. Ellis, Simulation and analysis of solenoidal ion sources, Rev. Sci. Instrum. 79 (2008) 123301. doi:10.1063/1.3030858.

[18] S.D. Eder, G. Bracco, T. Kaltenbacher, B. Holst, Two Dimensional Imaging of the Virtual Source of a Supersonic Beam: Helium at 125 K, J. Phys. Chem. A. 118 (2014) 4–12. doi:10.1021/jp4082855.

[19] A.S. Palau, G. Bracco, B. Holst, Theoretical model of the helium pinhole microscope, Phys. Rev. A. 94 (2016) 63624. doi:10.1103/PhysRevA.94.063624.

[20] A. Salvador Palau, G. Bracco, B. Holst, Theoretical model of the helium zone plate microscope, Phys. Rev. A. 95 (2017) 13611. doi:10.1103/PhysRevA.95.013611.

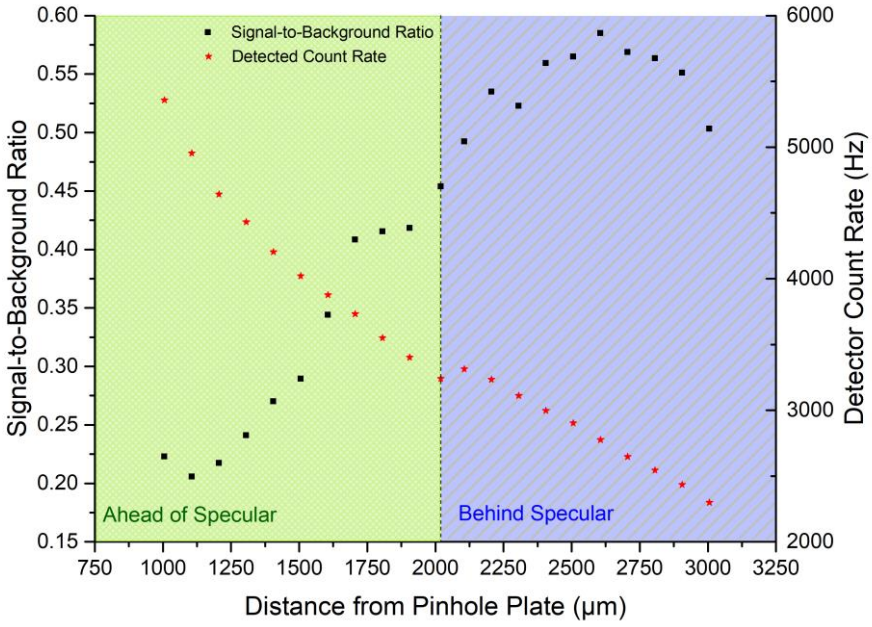

Fig. A.1. Plot of the detected helium count rate and instrument signal-to-background ratio for the SHeM, as collected using the 3D-printed step-height sample across a range of z-axis positions. The vertical dashed line indicates the specular plane of the instrument at a distance of 2020 microns from the pinhole plate, allowing distinction between positions ahead of and behind specular (see shaded regions).